Parametric conversion via second harmonic generation and two-hump solitons in phase-matched microresonators

Vladislav V. Pankratov and Dmitry V. Skryabin [*]

Department of Physics, University of Bath, Bath BA2 7AY, United Kingdom
and Centre for Photonics and Photonic Materials, University of Bath, Bath BA2 7AY, United Kingdom

Frequency conversion in microresonators has revolutionized modern-day nonlinear and quantum optics. Here, we present a theory of the multimode second harmonic generation in microresonators under conditions when the parametric conversion back to the pump spectrum dominates through the large domain in the resonator parameter space. We demonstrate that the spectral tunability of the sideband generation in this regime is governed by a discrete sequence of the so-called Eckhaus instabilities. We report the transition to mode locking and the generation of solitons, which have a double-pulse structure in the pump field. These solitons exist outside the bistability interval and on a slightly curved background.

I. INTRODUCTION

Frequency conversion and comb generation in optical resonators and microresonators are transforming the research and applications of nonlinear and quantum optics. They impact precision frequency metrology, mode locking, soliton photonics, and quantum and classical processing of information [1–3]. Microresonators made with the materials possessing the second-order, i.e., $\chi^{(2)}$, nonlinearity allow generating frequency combs at twice or half of the pump frequency at the comparatively low input powers, see, e.g., Refs. [4–9]. Another advantage of $\chi^{(2)}$ resonators is that the side-band generation relying on the $\chi^{(2)}$ effects does not critically depend on the dispersion sign, which facilitates working with visible and near-infrared sources. Though the generation of $\chi^{(2)}$ solitons in micro and bow-tie resonators has been demonstrated [7,10], it remains far from being as developed as the soliton techniques in Kerr resonators [11]. This, in its turn, hinders the development of applications of the $\chi^{(2)}$-based soliton mode locking in microresonators.

The initiation of the Kerr frequency comb happens via the generation of two weak side bands $\omega_{\pm\mu}$ from the two pump photons ω_p, i.e., $\hbar\omega_p + \hbar\omega_p = \hbar\omega_\mu + \hbar\omega_{-\mu}$, while the onset of the $\chi^{(2)}$-mediated side-band generation is more complex. Our recent analysis in Ref. [12] showed that the operator driving the initial stage of the second harmonic generation in the multimode $\chi^{(2)}$ resonators involved simultaneous and interdependent sum-frequency and parametric down-conversion terms. If the pump frequency is ω_p, then its second harmonic, $2\omega_p$, is allowed to down-convert via the parametric process to the two side bands of the pump field, i.e.,

$$\hbar 2\omega_p = \hbar\omega_{\mu a} + \hbar\omega_{-\mu a}. \tag{1}$$

Here and below, the subscripts a and b are used for the pump and second harmonic side bands, respectively. $\mu =$

0, ±1, ±2, . . . , numbers the side-band orders. The laser photon can also sum up with its own side band to generate side bands of the second harmonic, i.e.,

$$\hbar\omega_p + \hbar\omega_{\mu a} = \hbar\omega_{\mu b}. \tag{2}$$

The magnitude of the $\omega_{\mu a}$ to $\omega_{-\mu a}$ side-band coupling, controlling the rate of the parametric down-conversion in Eq. (1), is determined by the amplitude of the second harmonic, which is critically susceptible to the phase-matching. On the other hand, the magnitude of the $\omega_{\mu a}$ to $\omega_{\mu b}$ coupling, controlling the rate of the sum-frequency process in Eq. (2), is determined by the pump amplitude [12]. Thus, by tuning the phase-matching, one can adjust the balance between parametric and sum-frequency processes.

The authos of Ref. [12] considered the case when the sum-frequency dominated the parametric conversion. They featured the Rabi oscillations between the $\omega_{\mu a}$ and $\omega_{\mu b}$ states assisting with the quantum memory designs [13,14] and photon-photon polariton quasiparticles [15]. They also showed that the frequency comb generation thresholds and soliton existence conditions can be derived by applying the formalism of the dressed states similar to the two-level atom theory [12]. The present work is a companion to Ref. [12], where a comprehensive list of modern and historical references on $\chi^{(2)}$ effects in resonators can be found.

Here we deal with the resonator geometry as in Ref. [12], but consider the case of near phase-matching, such that the sum-frequency and parametric conversion rates become comparable. However, both rates are typically inferior to the much faster frequency scale set by the difference in the repetition rates of the first and second harmonics. This resonator operation condition is common in practice, see, e.g., Refs. [16,17], however, the theory for the multimode second-harmonic generation under such conditions remained unknown and is developed below.

The resonator considered here has ∼20 GHz repetition rate and ∼1 GHz repetition rate difference of the first and second

---
[*]d.v.skryabin@bath.ac.uk

harmonics, which implies that the initially overlapping ω_p and $2\omega_p$ pulses would be on opposite sides of the linear resonator only after a few tens of round trips. Since the repetition rate difference characterizes how fast the pulses walk away one from the other, it is called the walk-off parameter. The "walk-off" term is common and is also shared between the fiber and other resonator contexts, see, e.g., Refs. [18–21].

The methodology applied below is inherited from our recent theory of the parametric processes in the microresonator half-harmonic generation [22]. This approach relies on the slowly (relative to 1 GHz) varying amplitudes leading to the analytically solvable coupled-mode model. The two-color bright soliton pulses are hard to expect for such a large walk-off. However, they exist and have a two-hump structure in the pump field.

II. MODEL

We assume that the pump laser ω_p is tuned around the resonator mode with the frequency ω_{0a} so that the multimode intraresonator pump field and its second harmonic are expressed as

$$A e^{iM\vartheta - i\omega_p t} + \text{c.c.}, \quad A = \sum_\mu a_\mu(t) e^{i\mu\theta},$$

$$B e^{i2M\vartheta - i2\omega_p t} + \text{c.c.}, \quad B = \sum_\mu b_\mu(t) e^{i\mu\theta},$$

$$\theta = \vartheta - D_1 t. \tag{3}$$

Here M is the absolute mode number corresponding to the frequency ω_{0a}, $\vartheta = (0, 2\pi]$ is the angular coordinate, θ is the coordinate in the reference frame rotating with the user defined rate D_1, and $\mu = 0, \pm 1, \pm 2, \dots$, is the relative mode number. a_μ, b_μ are the amplitudes of the pump (fundamental) and second-harmonic modes. The respective resonator frequencies are

$$\omega_{\mu\zeta} = \omega_{0\zeta} + \mu D_{1\zeta} + \tfrac{1}{2}\mu^2 D_{2\zeta}, \quad \zeta = a, b, \tag{4}$$

where $D_{1\zeta}$ are the linear repetition rates and $D_{2\zeta}$ are dispersions. In what follows, we choose $D_1 = D_{1a}$. $D_{1b} - D_{1a}$ as the walk-off parameter, i.e., the repetition rate difference.

Coupled-mode equations governing the evolution of $a_\mu(t)$, $b_\mu(t)$ are [23]

$$i\partial_t a_\mu = \delta_{\mu a} a_\mu - \frac{i\kappa_a}{2}(a_\mu - \widehat{\delta}_{\mu,0}\mathcal{H})$$
$$- \gamma_a \sum_{\mu_1\mu_2} \widehat{\delta}_{\mu,\mu_1-\mu_2} b_{\mu_1} a_{\mu_2}^*,$$

$$i\partial_t b_\mu = \delta_{\mu b} b_\mu - \frac{i\kappa_b}{2} b_\mu - \gamma_b \sum_{\mu_1\mu_2} \widehat{\delta}_{\mu,\mu_1+\mu_2} a_{\mu_1} a_{\mu_2}, \tag{5}$$

where $\widehat{\delta}_{\mu,\mu'} = 1$ for $\mu = \mu'$ and is zero otherwise. $\mathcal{H}$ is the pump parameter under the critical coupling conditions, $\mathcal{H}^2 = \mathcal{F}\mathcal{W}/2\pi$, where $\mathcal{W}$ is the laser power and $\mathcal{F} = D_{1a}/\kappa_a$ is finesse. $\delta_{\mu\zeta}$ are the modal detuning parameters in the rotating reference frame, $\delta_{\mu a} = (\omega_{\mu a} - \tfrac{1}{2}\omega_p) - \mu D_{1a}$ and $\delta_{\mu b} = (\omega_{\mu b} - \omega_p) - \mu D_{1a}$. $\delta_{\mu\zeta}$ can be expressed via pump detuning δ_{0a} and the frequency-matching, i.e., phase-matching parameter ε [12]

TABLE I. Resonator and laser parameters used in this work. The values are representative for a whispering gallery LiNbO$_3$ microresonator pumped at $1\,\mu$m.

Linewidth: $\kappa_a/2\pi = 1$ MHz, $\kappa_b/2\pi = 4$ MHz

Pump finesse: $D_{1a}/\kappa_a = 20\,000$
Repetition rate difference: $(D_{1a} - D_{1b})/2\pi = 1$ GHz
Dispersion: $D_{2a}/2\pi = -100$ kHz, $D_{2b}/2\pi = -200$ kHz
Nonlinearity: $\gamma_a/2\pi = \gamma_b/2\pi = 300$ MHz/$\sqrt{\text{W}}$
Phase mismatch: $\varepsilon/2\pi$ between -50 and $+50$ MHz
Scaling of intraresonator power: $\mathcal{H}_*^2 = \kappa_a\kappa_b/\gamma_a\gamma_b = 44\,\mu$W
Laser power: $\mathcal{W}$ between $\sim 1\,\mu$W and ~ 1 mW

$$\varepsilon = 2\omega_{0a} - \omega_{0b},$$

$$\delta_{\mu a} = \omega_{0a} - \omega_p + \tfrac{1}{2}\mu^2 D_{2a}$$
$$= \delta_{0a} + \tfrac{1}{2}\mu^2 D_{2a},$$

$$\delta_{\mu b} = \omega_{0b} - 2\omega_p + \mu(D_{1b} - D_{1a}) + \tfrac{1}{2}\mu^2 D_{2b}$$
$$= 2\delta_{0a} - \varepsilon + \mu(D_{1b} - D_{1a}) + \tfrac{1}{2}\mu^2 D_{2b}. \tag{6}$$

We assume that the microresonator is made to operate close to phase-matching, $\varepsilon = 0$, while the repetition rate difference $D_{1b} - D_{1a}$ is the dominant frequency scale in Eq. (6), i.e.,

$$\mu|D_{1a} - D_{1b}| \gg |\varepsilon|, \quad \mu^2|D_{2\zeta}|, \quad \kappa_\zeta. \tag{7}$$

The parameter values used by us are typical for the LiNbO$_3$ whispering gallery microresonators [8,16] and are listed in Table I so that we can verify the validity of Eq. (7).

We now make the substitution

$$b_\mu(t) = B_\mu(t) e^{-i\mu(D_{1b} - D_{1a})t}, \quad \mu \neq 0, \tag{8}$$

where $B_\mu(t)$ are the slowly varying amplitudes relative to the fast oscillating exponent, and apply the slowly varying approximation by eliminating all the terms oscillating with the high frequencies; see the mathematical details in Ref. [22]. This procedure yields the following system of equations:

$$i\partial_t a_0 = \kappa_a \Delta_{0a} a_0 - \gamma_a b_0 a_0^* + \frac{i\kappa_a}{2}\mathcal{H}, \tag{9a}$$

$$i\partial_t a_\mu = \kappa_a \Delta_{\mu a} a_\mu - \gamma_a b_0 a_{-\mu}^*, \quad \mu \neq 0, \tag{9b}$$

$$i\partial_t a_{-\mu} = \kappa_a \Delta_{\mu a} a_{-\mu} - \gamma_a b_0 a_\mu^*, \tag{9c}$$

$$i\partial_t b_0 = \kappa_b \Delta_{0b} b_0 - \gamma_b a_0^2 - 2\gamma_b \sum_{\mu > 0} a_\mu a_{-\mu}. \tag{9d}$$

Figure 1 illustrates the dominant processes well described by Eq. (9). The second-harmonic sidebands, $b_{\mu \neq 0}$, are not featured in Eq. (9) and begin playing a role either in the higher-order approximations or if the assumptions in Eq. (7) are violated. The reduced model, Eq. (9), is applied below to derive the analytical results, while all the numerical data were generated using the master model Eq. (5).

The linear spectrum in Fig. 1 should be contrasted with the dressed, i.e., nonlinearity modified, spectrum implicated in the interplay of the Rabi oscillations and parametric processes studied in Ref. [12] and illustrated in their Fig. 6. Simultaneous parametric conversion and second-harmonic generation
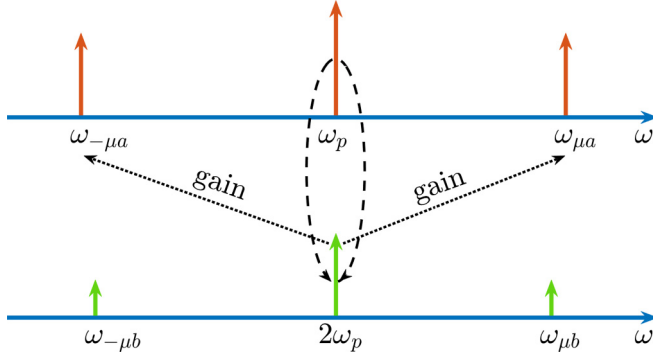
FIG. 1. Illustration of one of the parametric processes captured by the reduced model valid for $\mu|D_{1a} - D_{1b}| \gg |\varepsilon|$, see Eq. (9). It should be compared with the dressed state theory for $\mu|D_{1a} - D_{1b}| \sim |\varepsilon|$ illustrated by Fig. 6 in Ref. [12]. Here ε is the phase-matching parameter.

and other multistep $\chi^{(2)}$ frequency conversion schemes have a long history outside the comb context and continue to be explored currently [24–27].

Equation (9) and the text below use the $\Delta_{\mu\zeta}$ parameters, which are the auxiliary dimensionless detunings

$$\Delta_{\mu\zeta} = \left(\delta_{0\zeta} + \frac{1}{2}\mu^2 D_{2\zeta} - i\frac{1}{2}\kappa_\zeta\right)\frac{1}{\kappa_\zeta}. \tag{10}$$

Equation (10) includes the losses and, hence, $\Delta_{\mu\zeta}$ are complex-valued. We note that $\Delta_{\mu\zeta}$ are free from the walk-off parameter $D_{1b} - D_{1a}$, absorbed by the fast oscillating exponents in Eq. (8). The sum-frequency rate is determined by $\gamma_b|a_0|$, see Eq. (9d), and the rate of the parametric gain is $\gamma_a|b_0|$, see Eqs. (9a) to (9c), which are also assumed to comply with

$$\mu|D_{1a} - D_{1b}| \gg \gamma_a|b_0|, \quad \gamma_b|a_0|. \tag{11}$$

The difference between Eqs. (9a) to (9d) and the directly pumped optical parametric oscillator (OPO) model considered in Ref. [22] is in the moving the pumping term between the a_0 and b_0 equations. However, this change leads to a different and more involved theory than in Ref. [22]. On the other hand, the currently applied $\mu|D_{1a} - D_{1b}| \gg |\varepsilon|$ condition, see Eq. (7), simplifies the matters relative to the second-harmonic theory for $\mu|D_{1a} - D_{1b}| \sim |\varepsilon|$ developed in Ref. [12].

III. THEORY OF PARAMETRIC STATES

A. Homogeneous state

From the diversity of the possible solutions of Eqs. (9a) to (9d) the simplest one is the spatially homogeneous state with

$$A = \widetilde{a}_0, \quad B = \widetilde{b}_0. \tag{12}$$

We added the tildes here to introduce the notational difference with the $\mu = 0$ modes entering the OPO states introduced below and marked with the hats.

Setting the side-band amplitudes to zero, $a_\mu = 0$, the solution of Eq. (9d) is

$$\widetilde{b}_0 = \frac{\gamma_b\widetilde{a}_0^2}{\kappa_b\Delta_{0b}}. \tag{13}$$

Then, Eq. (9a) can be rearranged as

$$\left(\Delta_{0a} - \frac{|\widetilde{a}_0|^2}{\Delta_{0b}\mathcal{H}_*^2}\right)\frac{\widetilde{a}_0}{\mathcal{H}_*} = \frac{-i\mathcal{H}}{2\mathcal{H}_*}. \tag{14}$$

Here

$$\mathcal{H}_*^2 = \frac{\kappa_a\kappa_b}{\gamma_a\gamma_b} = 44\,\mu\text{W} \tag{15}$$

is the characteristic power introduced for normalization purposes. Taking the modulus squared of Eq. (14), we find the real cubic equation for $|\widetilde{a}_0|^2$,

$$\frac{|\widetilde{a}_0|^6}{\mathcal{H}_*^6} - 2\text{Re}(\Delta_{0a}\Delta_{0b})\frac{|\widetilde{a}_0|^4}{\mathcal{H}_*^4} + |\Delta_{0a}\Delta_{0b}|^2\frac{|\widetilde{a}_0|^2}{\mathcal{H}_*^2}$$
$$= \frac{\mathcal{H}^2|\Delta_{0b}|^2}{4\mathcal{H}_*^2}. \tag{16}$$

Examples of the dependencies of $\gamma_b|\widetilde{a}_0|$ (red lines) and $\gamma_a|\widetilde{b}_0|$ (green lines) versus the pump detuning δ_{0a} are shown in Figs. 2(a) to 2(c). One can see that the sum-frequency (red) and parametric (green) rates are of the same order. This should be compared with Fig. 1 in Ref. [12], where the phase-matching parameter was tuned to $|\varepsilon| \sim \mu|D_{1a} - D_{1a}|$ to achieve the sum-frequency rates dominating the parametric ones by two orders of magnitude.

B. Benjamin-Feir instabilities and emergence of OPO (Turing pattern) states

OPO states correspond to the resonator-generating one, or primarily one, side-band pairs in the pump field, i.e.,

$$A = \hat{a}_0 + a_\nu e^{i\nu\theta} + a_{-\nu}e^{-i\nu\theta}, \quad B = \hat{b}_0. \tag{17}$$

The OPO states are thus the simplest representatives of the Turing patterns, which are expected to bifurcate from the homogeneous state. Equations (9b) to (9d) are resolved as

$$a_\nu = |a_\nu|e^{i\phi_\nu}, \quad a_{-\nu} = |a_\nu|, \quad \hat{b}_0 = \frac{\Delta_{\nu a}\kappa_a}{\gamma_a}e^{i\phi_\nu}, \tag{18}$$

$$e^{i\phi_\nu} = \frac{\hat{a}_0^2/\mathcal{H}_*^2}{\Delta_{0b}\Delta_{\nu a} - 2|a_\nu|^2/\mathcal{H}_*^2}. \tag{19}$$

We note that the homogeneous state is the same for the master Eq. (5) and reduced, Eq. (9), models, but the above OPO states are exact for the reduced and approximate the master model.

The modulus squared of Eq. (19) yields the quadratic equation for the sideband amplitudes expressing $|a_\nu|^2$ as a function of $|\hat{a}_0|^2$,

$$\frac{|a_\nu|^2}{\mathcal{H}_*^2} = \frac{\text{Re}(\Delta_{\nu a}\Delta_{0b})}{2} + \frac{(-1)^j}{2}\sqrt{|\hat{a}_0|^4/\mathcal{H}_*^4 - \text{Im}^2(\Delta_{\nu a}\Delta_{0b})},$$
$$j = 0, 1, \tag{20}$$

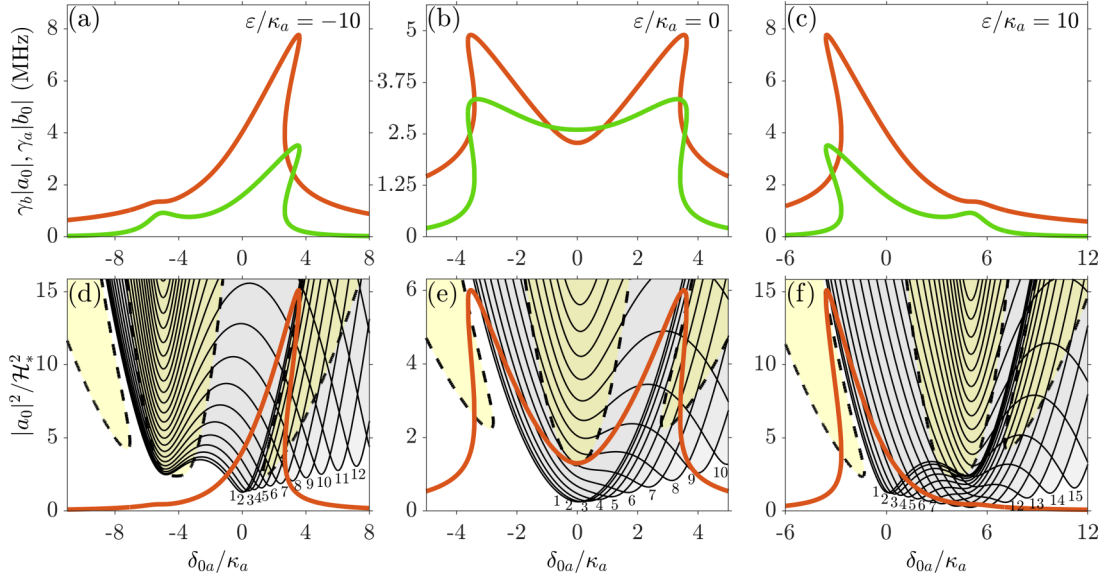where the value of $|\hat{a}_0|^2$ remains unknown and will be determined in Sec. III C.

FIG. 2. (a)–(c) Amplitudes of the homogeneous (single-mode) states vs detuning for the negative, zero, and positive values of the phase-mismatch parameter ε. The red (dark gray) lines mark $\gamma_b|\widetilde{a}_0|$, which is the rate of the sum-frequency process. The green (light gray) lines mark $\gamma_a|\widetilde{b}_0|$, which is the rate of the parametric process. Laser power is $\mathcal{W} = 0.7\,\mu\text{W}$, which corresponds to $\mathcal{H}^2/\mathcal{H}_*^2 = 50$. (d)–(f) Instability boundaries of the homogeneous state. The black lines $|a_0|^2 = |\hat{a}_{0,\text{th}}^{(\mu)}|^2$ and gray areas show the $\mu \neq 0$ Benjamin-Feir instabilities. The dashed black lines and yellow (light gray) shading show the $\mu = 0$ instabilities. Homogeneous state becomes unstable, when the red (gray) line $|a_0|^2 = |\widetilde{a}_0|^2$ crosses any of the thresholds.

Setting side-band powers to zero, $|a_\nu|^2 = 0$ in Eq. (20), we find

$$\frac{\left|\hat{a}_{0,\text{th}}^{(\nu)}\right|^2}{\mathcal{H}_*^2} = |\Delta_{0b}\Delta_{\nu a}|, \tag{21}$$

which gives a sequence of $|\hat{a}_{0,\text{th}}^{(\nu)}|^2$ versus δ_{0a} lines for all possible $\nu \neq 0$ corresponding to the thresholds where the OPO states (Turing patterns) bifurcate from the no-OPO (homogeneous) state. Thus, condition

$$|\widetilde{a}_0|^2 = \left|\hat{a}_{0,\text{th}}^{(\nu)}\right|^2 \tag{22}$$

gives the mode-number-specific Benjamin-Feir bifurcation thresholds of the homogeneous state. Figures 2(d) to 2(f) show how the $|a_0|^2 = |\widetilde{a}_0|^2$ versus δ_{0a} line intersects with a sequence of the $|a_0|^2 = |\hat{a}_{0,\text{th}}^{(\nu)}|^2$ lines. Each intersection point of the red and gray lines corresponds to the threshold detuning for generating the corresponding side-band pair.

We recall that the theory of this section is applicable for $\mu \neq 0$. To find the $\mu = 0$ instability boundary and verify the theory's results for $\mu \neq 0$, we linearized the master model Eq. (5) around the homogeneous state. To achieve this we assumed [12]

$$A = \widetilde{a}_0 + x_{\mu a}e^{\lambda_\mu t + i\mu\theta} + y_{\mu a}^* e^{\lambda_\mu t - i\mu\theta},$$
$$B = \widetilde{b}_0 + x_{\mu b}e^{\lambda_\mu t + i\mu\theta} + y_{\mu b}^* e^{\lambda_\mu t - i\mu\theta}. \tag{23}$$

Here $\vec{x}_\mu = (x_{\mu a}, x_{\mu b}, y_{\mu a}, y_{\mu b})^T$ is the perturbation vector and $\text{Re}\lambda_\mu$ is the instability growth rate. The resulting eigenvalue

problem for $\vec{x}_\mu$ is

$$i\lambda_\mu \vec{x}_\mu$$
$$= \begin{bmatrix} \delta_{\mu a} - \frac{i\kappa_a}{2} & -\gamma_a\widetilde{a}_0^* & -\gamma_a\widetilde{b}_0 & 0 \\ -2\gamma_b\widetilde{a}_0 & \delta_{\mu b} - \frac{i\kappa_b}{2} & 0 & 0 \\ \gamma_a\widetilde{b}_0^* & 0 & -\delta_{-\mu a} - \frac{i\kappa_a}{2} & \gamma_a\widetilde{a}_0 \\ 0 & 0 & 2\gamma_b\widetilde{a}_0^* & -\delta_{-\mu b} - \frac{i\kappa_b}{2} \end{bmatrix} \vec{x}_\mu. \tag{24}$$

The above matrix makes it obvious that $\widetilde{b}_0$ couples the a side-bands and drives the parametric conversion, see Eq. (1), and $\widetilde{a}_0$ provides the a to b coupling and drives the sum-frequency process, see Eq. (2). The $\text{Re}\lambda_0 = 0$ instability boundary is shown in Figs. 2(d) to 2(f) with the dashed-black lines and yellow shading. The $\text{Re}\lambda_{\mu \neq 0} = 0$ Benjamin-Feir instability boundaries found from Eq. (24) and derived from Eq. (22) cannot be distinguished; see the full-black lines and gray shading in Figs. 2(d) to 2(f).

We recall that the $\delta_{\mu\zeta}$ detunings in Eq. (24) include the walk-off parameter, see Eq. (6). $\delta_{\mu\zeta}$ should be compared with the walk-free $\Delta_{\mu\zeta}$, see Eq. (10), used to get our analytical results. Thus, we are dealing with a case where the large walk-off does not play a role in destabilizing the homogeneous state, cf. Ref. [19]. The independence of the instabilities from walk-off agrees with the fact that the second-harmonic field remains quasi-monochromatic, see Fig. 3(b), and hence should not be subjected to the group-velocity-related effects.

Figures 3(a) and 3(b) show the data from the numerical simulation of the master model, Eq. (5), for the fixed input power and varying detuning. Comparing the pump and second-harmonic spectra confirms our analytical result that the second harmonic sidebands are tiny and the ones in the
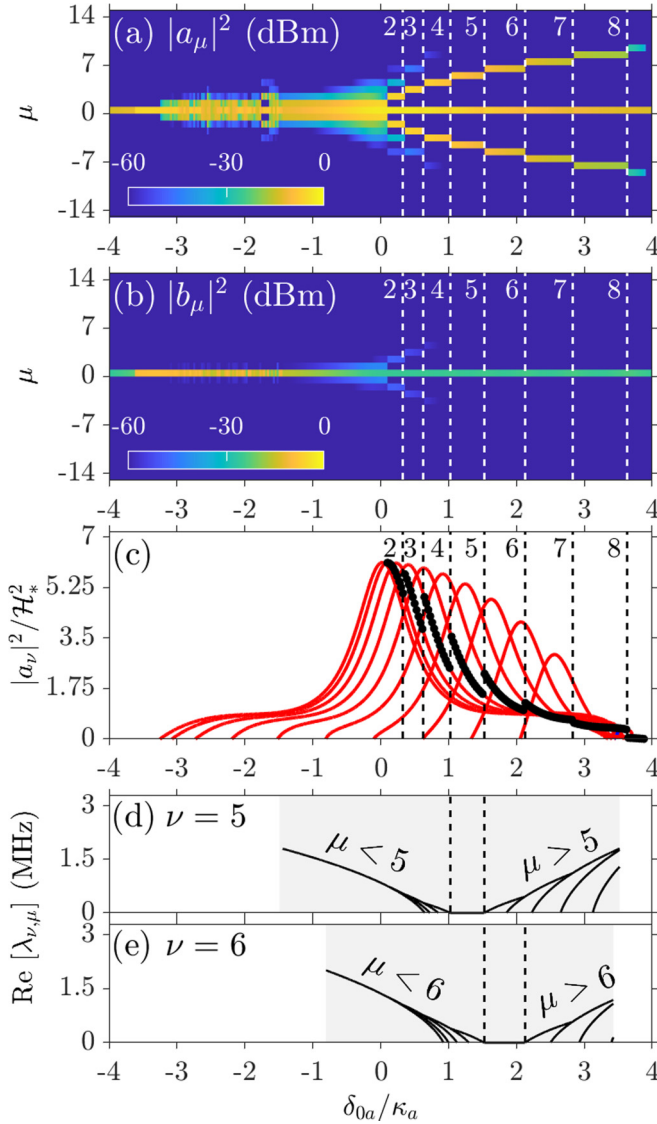
FIG. 3. (a,b) Results of dynamical simulations of Eq. (5). Panel (a) shows the mode number spectrum for the pump and panel (b) for the second harmonic field $\mathcal{H}^2/\mathcal{H}_*^2 = 50$ ($\mathcal{W} \approx 0.7\,\mu\mathrm{W}$), $\varepsilon = 0$. (c) Side-band amplitudes of the pump field found using Eq. (20) [red (gray) lines] and from the data in the panel (a) (black circles). (d,e) Eckhaus instability growth rates $\lambda_{\nu,\mu}$ for the $\nu = 5$ and $\nu = 6$ OPO states. The OPO states exist in the shaded area and are stable between the dashed lines.

pump are much stronger. This illustrates the essence of what we term the second-harmonic-driven parametric conversion. The transition to a sequence of the OPO states for $\delta_{0a} > 0$ is evident from the data in Fig. 3(a). One could plausibly assume that, as in a directly pumped OPO [22], the switching between the different OPO states is governed by the Eckhaus instabilities of the OPO states and not by the Benjamin-Feir bifurcations of the homogeneous state, see Sec. IV for details.

C. Super and subcritical bifurcations

The OPO (Turing pattern) states can emerge either super or subcritically at their bifurcation points from the homogeneous
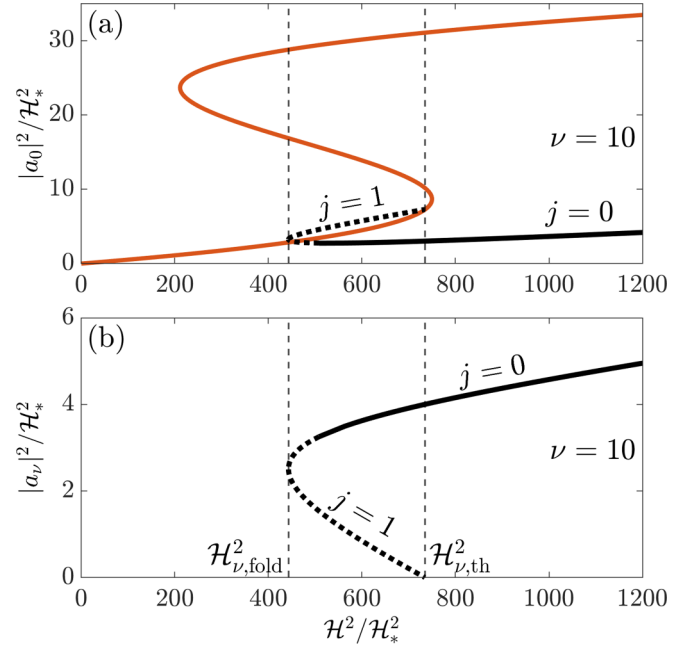

FIG. 4. Subcritical bifurcation of the OPO state, when the pump power is used as a control parameter: $\nu = 10$, $\delta_{0a}/\kappa_a = 7$, $\varepsilon = 0$. (a) The black line shows the zero-mode power $|\hat{a}_0|^2$ for the OPO state, see Eq. (26). The red (gray) line shows the power of the homogeneous state $|\widetilde{a}_0|^2$. (b) The OPO sideband power $|\hat{a}_{10}|^2$ vs pump. The full and dotted parts of the black lines in (a) and (b) correspond to $j = 0$ and $j = 1$ in Eq. (20).

state. Substituting $\hat{b}_0$ and $e^{i\phi_\nu}$ from Eqs. (18) and (19) in Eq. (9a) and rearranging, we find

$$\left(\Delta_{0a} - \frac{\Delta_{\nu a}|\hat{a}_0|^2/\mathcal{H}_*^2}{\Delta_{\nu a}\Delta_{0b} - 2|a_\nu|^2/\mathcal{H}_*^2} \right) \frac{\hat{a}_0}{\mathcal{H}_*} = \frac{-i\mathcal{H}}{2\mathcal{H}_*}. \tag{25}$$

Comparing the above and Eq. (14), we immediately see that they predictably coincide for $|a_\nu|^2 = 0$, i.e., $\hat{a}_0 = \widetilde{a}_0$ at the bifurcation points. Taking the modulus squared of Eq. (25) and using Eq. (20) for $|a_\nu|^2$ gives an explicit dependence of $\mathcal{H}^2/\mathcal{H}_*^2$ versus $|\hat{a}_0|^2$ for the Turing pattern states, see Fig. 4(a) for the $\nu = 10$ case. Substituting the $|\hat{a}_0|^2$ versus $\mathcal{H}^2/\mathcal{H}_*^2$ data set in Eq. (20) makes up the corresponding side-band powers, see Fig. 4(b). The transition between the full and dotted red lines in Fig. 4 shows how the $j = 0$ and $j = 1$ realizations of Eq. (20) play a role in constructing the complete branch of the Turing pattern.

The fact that the Turing pattern branch folds at $\mathcal{H}^2 = \mathcal{H}_{\nu,\mathrm{fold}}^2$, see Fig. 4(b), points that the patterns can bifurcate from the homogeneous state either super (no fold) or subcritically. In the second case, a range exists in the parameter space where a given side band ν can have two different powers, with the lower one never being stable. Quite remarkably, the fold condition and the Turing-pattern solutions can be expressed explicitly via the resonator parameters.

Computer algebra helps to demonstrate that Eqs. (25) and (20) reduce to a quadratic equation for $|\hat{a}_0|^2$,

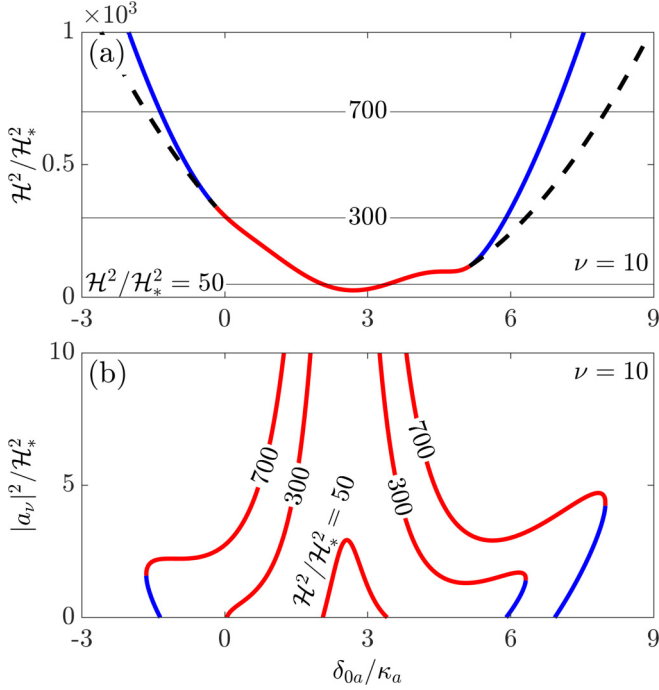$$Q_2 \frac{|\hat{a}_0|^4}{\mathcal{H}_*^4} + Q_1 \frac{|\hat{a}_0|^2}{\mathcal{H}_*^2} + Q_0 = 0, \tag{26}$$

FIG. 5. (a) The range of existence of the $\nu = 10$ OPO state in the pump power-detuning parameter space. The red or blue (gray or dark gray) lines correspond to the supercritical or subcritical bifurcation. The dashed line is the fold condition, see Eq. (28) and Fig. 4(b), where the two OPO states merge. (b) Powers of the OPO sidebands vs detuning for three selected pump powers: $\mathcal{H}^2/\mathcal{H}_*^2 = 50$ ($\mathcal{W} \approx 0.7\,\mu\text{W}$), $\mathcal{H}^2/\mathcal{H}_*^2 = 300$ ($\mathcal{W} \approx 4\,\mu\text{W}$), $\mathcal{H}^2/\mathcal{H}_*^2 = 700$ ($\mathcal{W} \approx 9\,\mu\text{W}$).

where

$$Q_2 = (|\Delta_{0a}|^2 + |\Delta_{va}|^2)^2 - 4\text{Re}^2(\Delta_{0a}\Delta_{va}{}^*),$$

$$Q_1 = (|\Delta_{0a}|^2 + |\Delta_{va}|^2)$$

$$\times \left(4\text{Im}(\Delta_{0b}\Delta_{va})\text{Im}(\Delta_{0a}\Delta_{va}^*) - \frac{\mathcal{H}^2}{2\mathcal{H}_*^2}\right),$$

$$Q_0 = \text{Im}(\Delta_{0b}\Delta_{va})\left(4|\Delta_{0a}\Delta_{va}|^2\text{Im}(\Delta_{0b}\Delta_{va})\right.$$

$$\left. -\text{Im}(\Delta_{0a}\Delta_{va}^*)\frac{\mathcal{H}^2}{2\mathcal{H}_*^2}\right) + \frac{\mathcal{H}^4}{16\mathcal{H}_*^4}. \tag{27}$$

A pair of solutions of Eq. (26) degenerate when the discriminant becomes zero, i.e., $Q_1^2 = 4Q_0Q_2$, which opens up as

$$\frac{\mathcal{H}_{v,\text{fold}}^4}{\mathcal{H}_*^4} - 16\text{Im}(\Delta_{0b}\Delta_{va})\text{Im}(\Delta_{0a}\Delta_{va}^*)\frac{\mathcal{H}_{v,\text{fold}}^2}{\mathcal{H}_*^2}$$

$$- 16(|\Delta_{0a}|^2 - |\Delta_{va}|^2)^2\text{Im}^2(\Delta_{0b}\Delta_{va}) = 0. \tag{28}$$

Equation (28) corresponds to the fold line in the parameter space.

The diagrams in Figs. 2(d) and 2(e) are plotted for the intraresonator mode power varying with detuning while the laser power is kept fixed. Expressing thresholds in terms of the laser power is also possible. Substituting Eq. (22) in Eq. (16) and using Eq. (21), provides the threshold values of
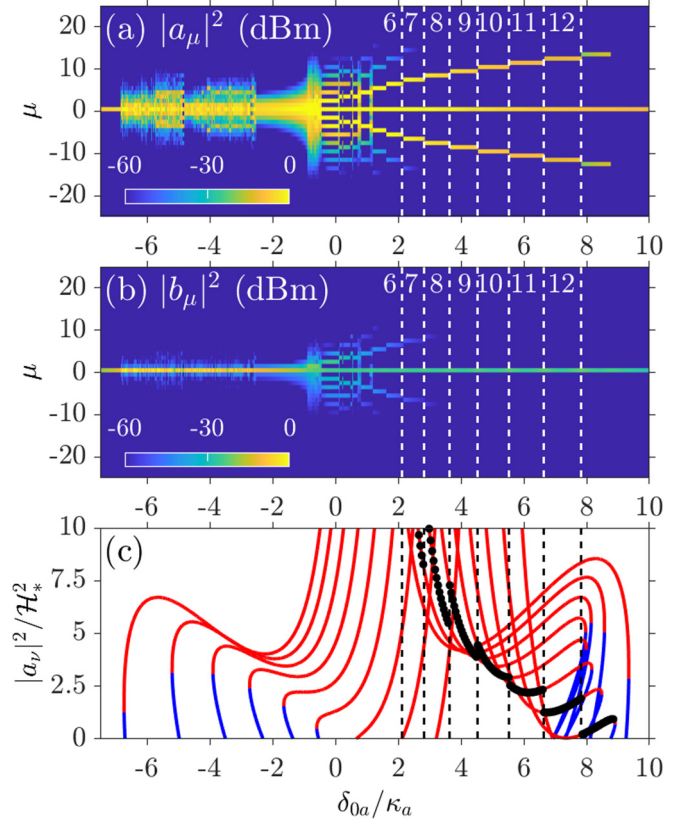

FIG. 6. (a,b) Results of dynamical simulations of Eq. (5). Panel (a) shows the mode number spectrum for the pump and panel (b) for the second harmonic field $\mathcal{H}^2/\mathcal{H}_*^2 = 700$ ($\mathcal{W} \approx 9\,\mu\text{W}$), $\varepsilon = 0$. (c) Side-band amplitudes of the pump field found using Eq. (20) [red (gray) and blue (dark gray) lines] and from the data in the panel (a) (black circles).

the laser power

$$\frac{\mathcal{H}_{v,\text{th}}^2}{\mathcal{H}_*^2} = 4|\Delta_{0b}\Delta_{va}|(|\Delta_{0a}|^2 + |\Delta_{va}|^2)$$

$$- 8\text{Re}(\Delta_{0b}\Delta_{0a})|\Delta_{va}|^2. \tag{29}$$

The fold line $\mathcal{H}^2 = \mathcal{H}_{v,\text{fold}}^2$ splits from the threshold condition $\mathcal{H}^2 = \mathcal{H}_{v,\text{th}}^2$ at the points where the bifurcation changes from super to subcritical, see Fig. 5(a).

The detuning dependencies of the side-band amplitudes in Fig. 5(b) show in an obvious way how the supercritical bifurcations change to subcritical as the pump power is increased. Figure 3(c) compares the analytical side-band amplitudes (red lines) with the ones found from the numerical modeling of the master equation. Figure 6 extends this comparison to the higher powers, where the OPO bifurcations become subcritical.

IV. ECKHAUS INSTABILITIES

Figures 3 and 6 show that as detuning approaches zero and crosses to the positive values, the resonator enters a regime of the operation characterized by the ladder-like transitions between the sequential OPO states, see Eq. (17). Points where one state switches to the next correspond to
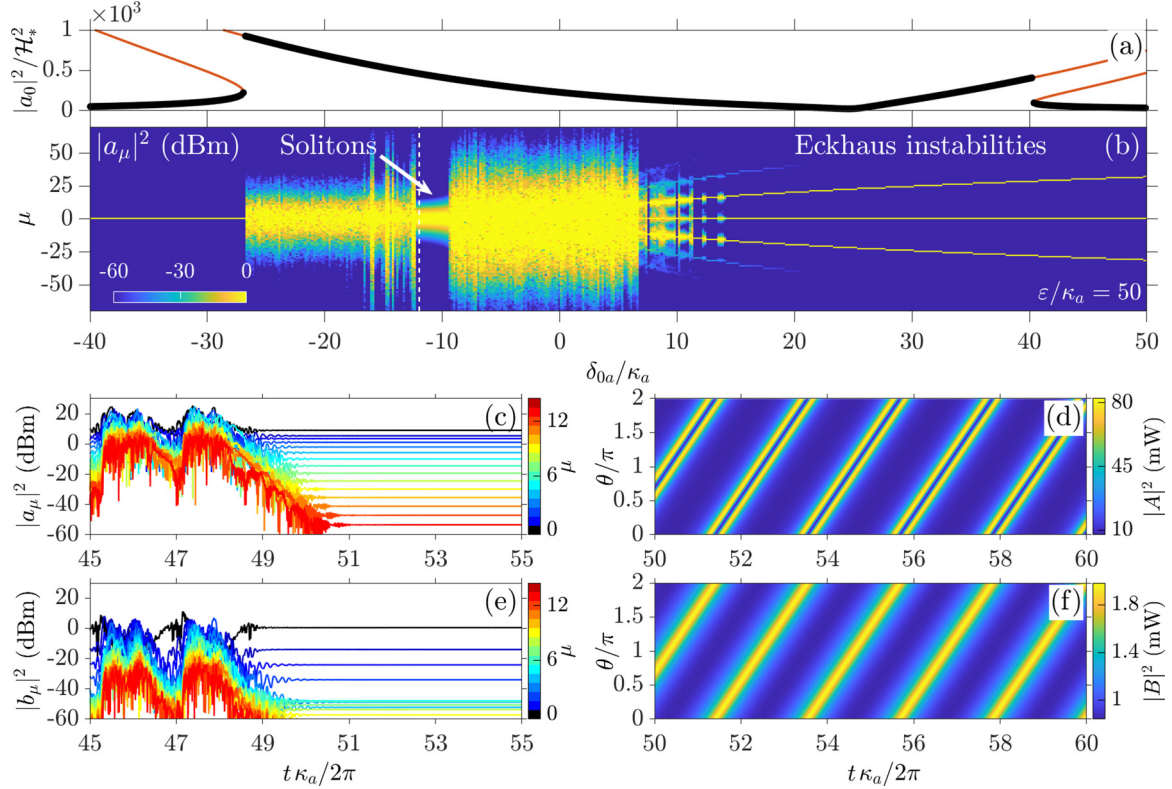
FIG. 7. (a,b) Detuning scan data and (c)–(f) the soliton modelocking data for $\varepsilon/\kappa_a = 50$, $\mathcal{H}^2/\mathcal{H}_*^2 = 310\,000$ ($\mathcal{W} = 4\,\text{mW}$), see Eq. (5). Panel (a) shows the bistability of the homogeneous state. Black points indicate solutions used as initial conditions for data in (b). (c,e) transition to mode locking for the detuning marked by the dashed white line in panel (b). The color bars show the mode numbers, $\mu = 0, 1, \ldots, 16$. Panels (d,f) show the space-time evolution of the soliton in the reference frame rotating with the rate D_{1a}. The color bars show the intraresonator power for (d) the pump and (f) second harmonic.

the Eckhaus instabilities, i.e., to the instabilities of the $\hat{a}_{0,\nu} + a_\nu e^{i\nu\theta} + a_{-\nu} e^{-i\nu\theta}$ pattern relative to $\hat{a}_{0,\nu+1} + a_{\nu+1} e^{i(\nu+1)\theta} + a_{-(\nu+1)} e^{-i(\nu+1)\theta}$ [22]. Here, we added the subscript ν, $\hat{a}_0 \to \hat{a}_{0,\nu}$, $\hat{b}_0 \to \hat{b}_{0,\nu}$, to indicate explicitly that the amplitude of the zero mode in an OPO state depends on the order ν of the side bands involved; see Eqs. (26) and (27) for $\hat{a}_0$ and Eq. (18) for $\hat{b}_0$. The authors of Refs. [28,29] provided discussions and comprehensive overviews of the Eckhaus instabilities in optical systems using an assumption of the unbounded geometry, while the authors of Ref. [22] and those of the present manuscript use the coupled-mode theory capturing the finite-size effects important in microresonators.

We now consider the $\pm\mu$ side-band pair as a small perturbation disturbing the OPO state of order ν. $\nu \neq 0$ corresponds to an OPO state with $b_0 = \hat{b}_{0,\nu}$ and $\nu = 0$ to the homogeneous state $b_0 = \tilde{b}_0$. An equation for the instability growth rate is then easily derived from Eqs. (9b) and (9c) applying the substitution $a_\mu(t) = x_{\mu a} e^{t\lambda_{\nu,\mu}}$ and $a_{-\mu}^*(t) = x_{-\mu a} e^{t\lambda_{\nu,\mu}}$,

$$\lambda_{\nu,\mu} = -\tfrac{1}{2}\kappa_a + \sqrt{\gamma_a^2 |b_0|^2 - \kappa_a^2 |\Delta_{\mu a}|^2}, \quad \mu \neq 0. \tag{30}$$

For $\nu = 0$ (Benjamin-Feir instability), we shall apply $|b_0|^2 = |\tilde{b}_0|^2 = \gamma_b^2 |\tilde{a}_0|^4 / \kappa_b^2 |\Delta_{0b}|^2$. Here, $|\tilde{a}_0|^2$ is a function of the laser power $\mathcal{H}^2$, see Eq. (14). For $\nu \neq 0$ (Eckhaus instability), $|b_0|^2 = |\hat{b}_{0,\nu}|^2 = \kappa_a^2 |\Delta_{\nu a}|^2 / \gamma_a^2$, which does not explicitly involve $\mathcal{H}^2$. We should, however, stress that the range of

existence of $|a_\nu|^2 > 0$ and, hence, of $\hat{b}_{0,\nu}$ (via its phase) is power dependent, see Eq. (19) and Fig. 5(b).

The growth rate of the Eckhaus instabilities, i.e., $\nu \neq 0$, of the OPO states simplifies to

$$\lambda_{\nu,\mu} = -\tfrac{1}{2}\kappa_a + \kappa_a \sqrt{|\Delta_{\nu a}|^2 - |\Delta_{\mu a}|^2}$$

$$= -\tfrac{1}{2}\kappa_a + \sqrt{\left(\delta_{0a} + \tfrac{1}{2}D_{2a}\nu^2\right)^2 - \left(\delta_{0a} + \tfrac{1}{2}D_{2a}\mu^2\right)^2}. \tag{31}$$

The Eckhaus instability rates for the $\nu = 5$ and $\nu = 6$ OPO states versus detuning are shown in Figs. 3(d) and 3(e), respectively. The intervals of stability match the results of dynamical simulations; see the vertical dashed lines in Figs. 3 and 6, which are derived from the conditions $\text{Re}\,\lambda_{\nu,\nu\pm1} = 0$.

Thus, we demonstrated that the OPO tuning from one mode pair to the other is underpinned by a sequence of Eckhaus instabilities developing for positive detunings. Changing dispersion at the pump frequency to anomalous $D_{2a} > 0$ moves the Eckhaus range to the negative detunings.

V. TWO-HUMP SOLITONS

The spectra in Fig. 6(a) correspond to the chaotic dynamics if $-7 \lesssim \delta_{0a}/\kappa_a \lesssim -3$, while for $-3 \lesssim \delta_{0a}/\kappa_a \lesssim 0$, the resonator enters mode locking. Further system-
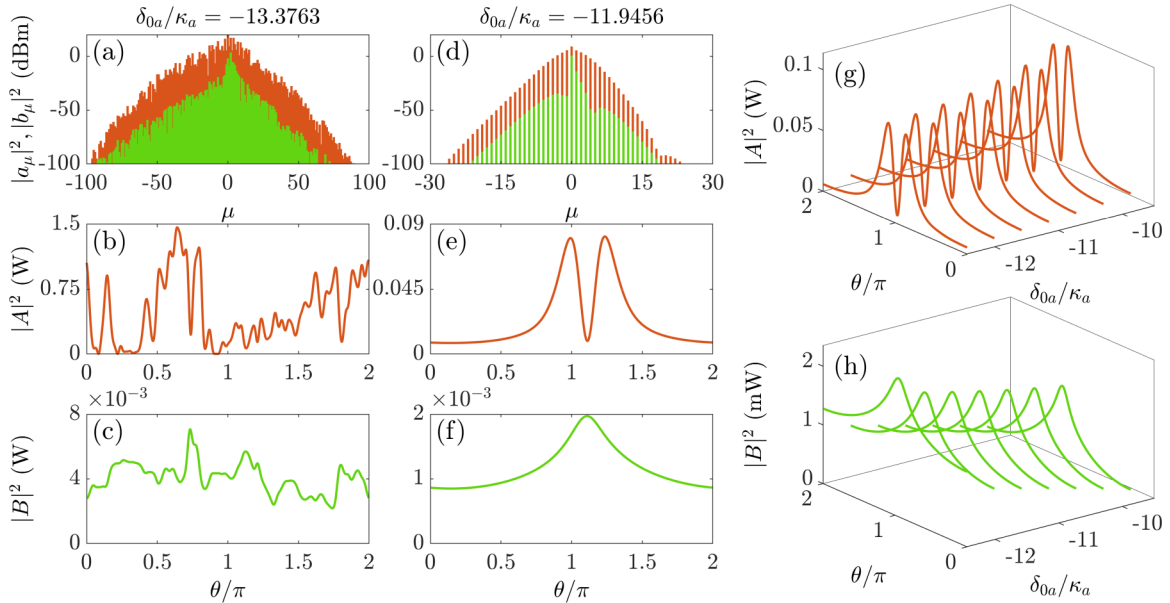
FIG. 8. Details of the spectra and spatial profiles of the pump [red (gray)] and second harmonic [green (light gray)] (a)–(c) outside and (d)–(f) inside the soliton modelocking interval. Panels (g,h) show how the spatial soliton profile varies with detuning. The system parameters are as in Fig. 7.

atic numerical exploration of the mode locking revealed that the higher powers bring more modes to the phase-locked state, which corresponds to a train of the soliton pulses.

Figures 7–9 show the data sets we generated solving the master model, Eq. (5), for the laser power $\mathcal{W} = 4$ mW and three different values of the phase-mismatch parameter $\varepsilon/\kappa_a = +50$ (Figs. 7 and 8), $\varepsilon/\kappa_a = -50$ [Fig. 9(b)], and $\varepsilon/\kappa_a = 0$ [Fig. 9(d)]. For all three cases, we found the range of the negative detunings located between the two tilted resonances of the homogeneous state, where the chaotic multimode dynamics cease to exist and is replaced by mode locking and soliton formation. The numerical simulations were initialized by the noise on top of the homogeneous states; see the black crosses along the red lines in Figs. 7(a), 9(a), and 9(c). For positive detuning, all homogeneous states are unstable, and independently from the initial condition, the system converges to the sequence of the Eckhaus instabilities. For negative detuning, the low-power homogeneous state is mostly stable, and therefore, the resonator transits to chaos after the bistability range ends.

Dynamically, the transition from chaos to mode locking happens after sufficiently long simulation times that have typically been extended to one or a few hundreds of photon lifetimes, $2\pi/\kappa_a$. The emergence of mode locking for the modes $\mu = 0, 1, 2, \ldots, 16$ is shown in Figs. 7(c) and 7(e). The space-time shapes of the mode-locked soliton pulses are shown in Figs. 7(d) and 7(f) and Figs. 8(e) to 8(h). The soliton in the pump field has two humps, while the single pulse in the second harmonic is centered between them. The solitons can be compared with the chaotic waveforms shown in Figs. 8(a) to 8(c).

The spectral shape of the pump component of the soliton is a typical soliton spectrum, which gradually decays as μ moves away from the center; see Figs. 7(c) and 8(d). The spectrum

of the second harmonic is, however, different. Its only significant modes are $\mu = 0, 1, 2$, and, perhaps, 3; see Figs. 7(e) and 8(d). It prompts a hypothesis that the soliton could be qualitatively considered as a broadband pump pulse supported by the effective potential created by the few dominant modes in the second harmonic field. These modes are near-phase-matched, and therefore, are subjected to the optical Pockels effect [12,30]. On the contrary, the solitons' spectral tails are phase-mismatched via growing $\mu|D_{1a} - D_{ab}|$, and therefore, experience the effective (cascaded) Kerr nonlinearity [12,22]. The pronounced spectral reshaping around $\mu = 0$, see Fig. 8(d), signals the transition between the Pockels and Kerr nonlinearities. The spectral tails are generated via the frequency-sum and frequency-difference terms entering the sums in the master model, see Eq. (5), and neglected in the approximate theory describing the OPO regime, see Eq. (9).

The solitons reported here have further features different from what is commonly known for solitons in optical resonators. First, these solitons are shifted well outside the bistability of the homogeneous state and are located between the two bistability intervals. Increasing ε, and depending on its sign, begins destroying the bistability for either negative or positive detunings, see Fig. 3, and shrinks the range where solitons are observed. For $|\varepsilon|$ becoming large, $|\varepsilon| \sim \mu|D_{1a} - D_{1b}|$, the other type of solitons emerges as demonstrated in Ref. [12]. The solitons in Ref. [12] are more conventional in the sense that they coexist with the bistability and are supported by the familiar interplay between dispersion and the effective Kerr effect, albeit derived via the dressed-state theory.

Another interesting property of the soliton profiles in Fig. 8 is that the finite-size effects responsible for the spectral discreteness, and therefore, making a difference between the frequency-comb solitons and the solitons with continuous
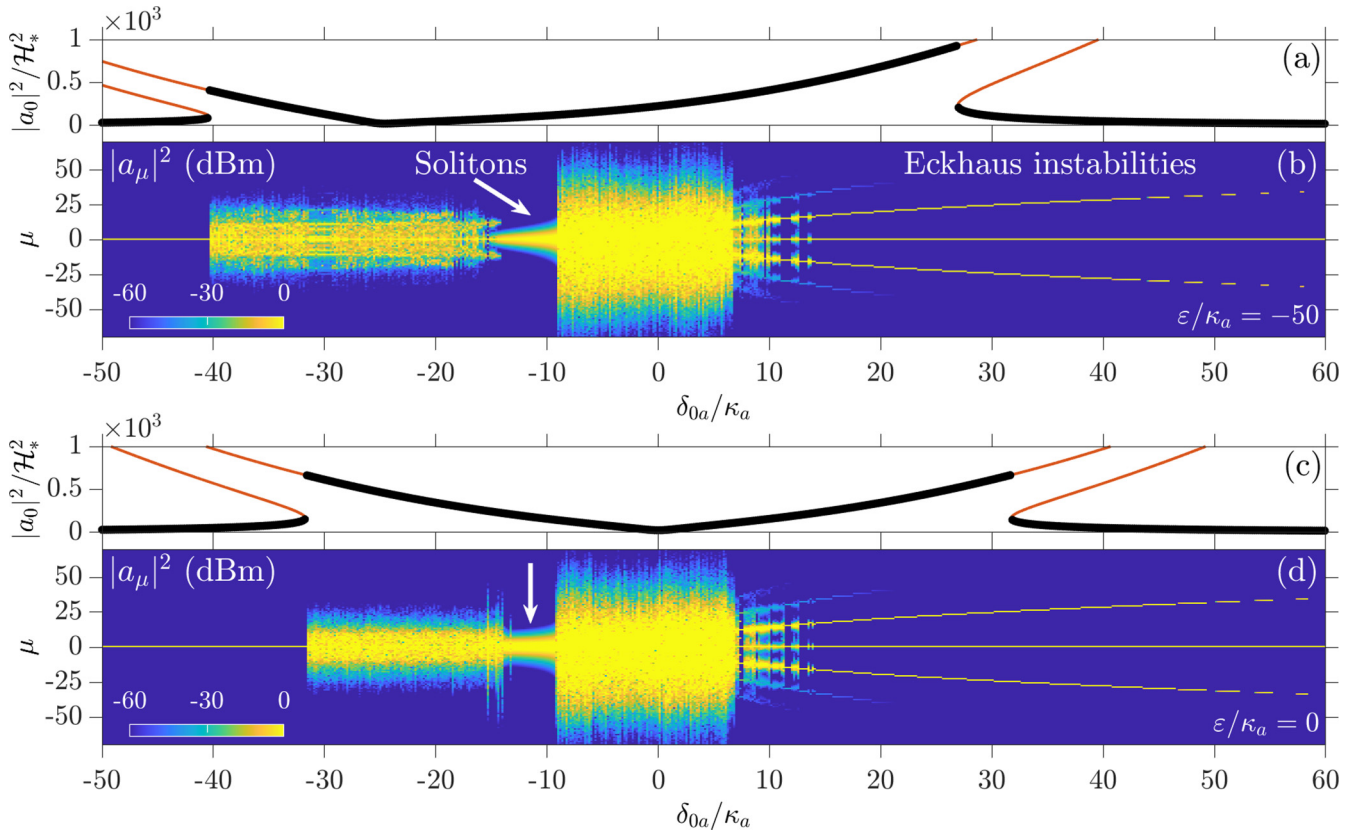
FIG. 9. Detuning scan data for (a,b) $\varepsilon/\kappa_a = -50$ and (c,d) $\varepsilon/\kappa_a = 0$: $\mathcal{H}^2/\mathcal{H}_*^2 = 310000$ ($\mathcal{W} = 4\text{mW}$), see Eq. (5). Panels (a,c) show the bistability of the homogeneous state. Black points indicate solutions used as initial conditions for data in (b,d).

spectra play a role here. In particular, one can see the soliton background is slightly curved. We checked that changing the dispersion sign to anomalous moves solitons to the positive detunings and keeps them outside the bistability range. We leave for future analysis the question of if the two-hump solitons found here connect or not to the solitons reported in Ref. [12] and an understanding of the full range of the soliton existence.

VI. SUMMARY

We presented a theory of parametric conversion via the second-harmonic generation in the phase-matched whispering gallery LiNbO$_3$ microresonators with large walk-off. The pump wavelength was assumed at one micron, so the dispersion was considered normal. The large walk-off condition, which means that the repetition rate difference is much larger than the phase-matching parameter $\mu|D_{1a} - D_{1b}| \gg \varepsilon$ applied in this work complements our recent study of the resonators with $\mu|D_{1a} - D_{1b}| \sim \varepsilon$, see Ref. [12]. Here μ is the relative mode number counted from the pump.

We demonstrated that tuning of the parametric signal and generation of side-band pairs around the pump is associated with the sequence of the Eckhaus instabilities happening for positive detunings. We derived a transparent approximate expression for the growth rates of the Eckhaus instabilities, see Eq. (31) and Fig. 3. A feature of these instabilities is their quasi-independence from the walk-off due to the second harmonic staying quasi-monochromatic and most of the spectrum generated in the pump field. We also found the side-band powers and identified conditions for the super and subcritical transitions to the OPO, i.e., Turing pattern, states. All these results are obtained under the conditions of the ring geometry, i.e., when the mode numbers are quantized.

The resonator operation regimes on the negative detuning side are more complex and often chaotic. However, we found an interval of negative detunings where the multimode chaos is replaced by mode locking. The mode locking leads to the soliton formation in the form of a double-hump pulse in the pump field and the single-hump pulse in the second harmonic. A distinct feature of these solitons is their size comparable to the resonator circumference. They exist on the nonflat background and outside the bistability range of the single-mode state. A spectrum of the pump component of the soliton has a typical near-triangular shape, while only a few first modes dominate the second-harmonic component.

Data presented in this study are openly available from the University of Bath Research Data Archive [31].

[1] A. Pasquazi, M. Peccianti, L. Razzari, D. J. Moss, S. Coen, M. Erkintalo, Y. K. Chembo, T. Hansson, S. Wabnitz, P. Del'Haye, X. Xue, A. M. Weiner, and R. Morandotti, Microcombs: A novel generation of optical sources, Phys. Rep. **729**, 1 (2018).

[2] M. A. Guidry, D. M. Lukin, K. Y. Yang, R. Trivedi, and J. Vuckovic, Quantum optics of soliton microcombs, Nat. Photonics **16**, 52 (2022).

[3] Y. Cai, J. Roslund, V. Thiel, C. Fabre, and N. Treps, Quantum enhanced measurement of an optical frequency comb, npj Quantum Inf. **7**, 82 (2021).

[4] V. Ulvila, C. R. Phillips, L. Halonen, and M. Vainio, Frequency comb generation by a continuous-wave-pumped optical parametric oscillator based on cascading quadratic nonlinearities, Opt. Lett. **38**, 4281 (2013).

[5] I. Ricciardi, S. Mosca, M. Parisi, F. Leo, T. Hansson, M. Erkintalo, P. Maddaloni, P. De Natale, S. Wabnitz, and M. De Rosa, Optical frequency combs in quadratically nonlinear resonators, Micromachines **11**, 230 (2020).

[6] X. Guo, C. L. Zou, H. Jung, Z. Gong, A. Bruch, L. Jiang, and H. X. Tang, Efficient Generation of a Near-visible Frequency Comb via Cherenkov-like Radiation from a Kerr Microcomb, Phys. Rev. Appl. **10**, 014012 (2018).

[7] A. W. Bruch, X. Liu, Z. Gong, J. B. Surya, M. Li, C. L. Zou, and H. Tang, Pockels soliton microcomb, Nat. Photonics **15**, 21 (2021).

[8] J. Szabados, D. N. Puzyrev, Y. Minet, L. Reis, K. Buse, A. Villois, D. V. Skryabin, and I. Breunig, Frequency Comb Generation Via Cascaded Second-Order Nonlinearities In Microresonators, Phys. Rev. Lett. **124**, 203902 (2020).

[9] N. Amiune, D. N. Puzyrev, V. V. Pankratov, D. V. Skryabin, K. Buse, and I. Breunig, Optical-parametric-oscillation-based chi(2) frequency comb in a lithium niobate microresonator, Opt. Express **29**, 41378 (2021).

[10] M. Jankowski, A. Marandi, C. R. Phillips, R. Hamerly, K. A. Ingold, R. L. Byer, and M. M. Fejer, Temporal Simultons in Optical Parametric Oscillators, Phys. Rev. Lett. **120**, 053904 (2018).

[11] T. J. Kippenberg, A. L. Gaeta, M. Lipson, and M. Gorodetsky, Dissipative Kerr solitons in optical microresonators, Science **361**, eaan8083 (2018).

[12] D. N. Puzyrev, V. V. Pankratov, A. Villois, and D. V. Skryabin, Bright-soliton frequency combs and dressed states in chi(2) microresonators, Phys. Rev. A **104**, 013520 (2021).

[13] X. Guo, C. L. Zou, H. Jung, and H. X. Tang, On-Chip Strong Coupling and Efficient Frequency Conversion between Telecom and Visible Optical Modes, Phys. Rev. Lett. **117**, 123902 (2016).

[14] M. Li, Y.-L. Zhang, H. X. Tang, C.-H. Dong, G.-C. Guo, and C.-L. Zou, Photon-Photon Quantum Phase Gate in a Photonic Molecule with $\chi^{(2)}$ Nonlinearity, Phys. Rev. Appl. **13**, 044013 (2020).

[15] D. V. Skryabin, V. V. Pankratov, A. Villois, and D. N. Puzyrev, Photon-photon polaritons in chi(2) microresonators, Phys. Rev. Res. **3**, L012017 (2021).

[16] J. Szabados, B. Sturman, and I. Breunig, Frequency comb generation threshold via second-harmonic excitation in chi(2) optical microresonators, APL Photonics **5**, 116102 (2020).

[17] J. Lu, A. Al Sayem, Z. Gong, J. B. Surya, C. L. Zou, and H. X. Tang, Ultralow-threshold thin-film lithium niobate optical parametric oscillator, Optica **8**, 539 (2021).

[18] D. V. Skryabin and A. R. Champneys, Walking cavity solitons, Phys. Rev. E **63**, 066610 (2001).

[19] F. Leo, T. Hansson, I. Ricciardi, M. De Rosa, S. Coen, S. Wabnitz, and M. Erkintalo, Walk-Off-Induced Modulation Instability, Temporal Pattern Formation, and Frequency Comb Generation in Cavity-Enhanced Second-Harmonic Generation, Phys. Rev. Lett. **116**, 033901 (2016).

[20] M. Zitelli, F. Mangini, M. Ferraro, O. Sidelnikov, and S. Wabnitz, Conditions for walk-off soliton generation in a multimode fiber, Commun. Phys. **4**, 182 (2021).

[21] A. Roy, R. Nehra, S. Jahani, L. Ledezma, C. Langrock, M. Fejer, and A. Marandi, Temporal walk-off induced dissipative quadratic solitons, Nat. Photonics **16**, 162 (2022).

[22] D. N. Puzyrev and D. V. Skryabin, Ladder of Eckhaus instabilities and parametric conversion in chi(2) microresonators, Commun. Phys. **5**, 138 (2022).

[23] D. V. Skryabin, Coupled-mode theory for microresonators with quadratic nonlinearity, J. Opt. Soc. Am. B **37**, 2604 (2020).

[24] M. E. Smithers and E. Y. C. Lu, Quantum theory of coupled parametric down-conversion and up-conversion with simultaneous phase matching, Phys. Rev. A **10**, 1874 (1974).

[25] D. V. Strekalov, A. S. Kowligy, V. G. Velev, G. S. Kanter, P. Kumar, and Y. P. Huang, Phase matching for the optical frequency conversion processes in whispering gallery mode resonators, J. Mod. Opt. **63**, 50 (2016).

[26] N. Flemens, N. Swenson, and J. Moses, Efficient parametric amplification via simultaneous second harmonic generation, Opt. Express **29**, 30590 (2021).

[27] W. R. Rowe, A. V. Gorbach, and D. V. Skryabin, Solitons near avoided mode crossings in chi(2) nanowaveguides, Phys. Rev. A **104**, 053510 (2021).

[28] S. Longhi, Travelling-wave states and secondary instabilities in optical parametric oscillators, Phys. Rev. A **53**, 4488 (1996).

[29] P. Parra-Rivas, D. Gomila, L. Gelens, and E. Knobloch, Bifurcation structure of periodic patterns in the Lugiato-Lefever equation with anomalous dispersion, Phys. Rev. E **98**, 042212 (2018).

[30] D. V. Skryabin, Sech-squared Pockels solitons in the microresonator parametric down-conversion, Opt. Express **29**, 28521 (2021).

[31] https://doi.org/10.15125/BATH-01201.

Correction: A conversion error introduced during the production process in Equation (16) has been fixed.